

Liquid-Metal-Enabled Mechanical-Energy-Induced CO₂ Conversion

Junma Tang, Jianbo Tang,* Mohannad Mayyas, Mohammad B. Ghasemian, Jing Sun, Md Arifur Rahim, Jiong Yang, Jialuo Han, Douglas J. Lawes, Rouhollah Jalili, Torben Daeneke, Maricruz G. Saborio, Zhenbang Cao, Claudia A. Echeverria, Francois-Marie Allieux, Ali Zavabeti, Jessica Hamilton, Valerie Mitchell, Anthony P. O'Mullane, Richard B. Kaner, Dorna Esrafilzadeh,* Michael D. Dickey, and Kourosch Kalantar-Zadeh*

A green carbon capture and conversion technology offering scalability and economic viability for mitigating CO₂ emissions is reported. The technology uses suspensions of gallium liquid metal to reduce CO₂ into carbonaceous solid products and O₂ at near room temperature. The nonpolar nature of the liquid gallium interface allows the solid products to instantaneously exfoliate, hence keeping active sites accessible. The solid co-contributor of silver–gallium rods ensures a cyclic sustainable process. The overall process relies on mechanical energy as the input, which drives nano-dimensional triboelectrochemical reactions. When a gallium/silver fluoride mix at 7:1 mass ratio is employed to create the reaction material, 92% efficiency is obtained at a remarkably low input energy of 230 kWh (excluding the energy used for dissolving CO₂) for the capture and conversion of a tonne of CO₂. This green technology presents an economical solution for CO₂ emissions.

1. Introduction

Innovative technologies are urgently demanded for capturing and converting CO₂ into value-added species, at low input energy, to mitigate the negative effects of this greenhouse gas and support a sustainable carbon cycle.^[1,2] Activating CO₂ into CO₂^{•-} radicals or other intermediates is a crucial step for CO₂ conversion, while the inertness of CO₂ molecules imposes a significant challenge.^[3] To this end, external energy is required, and catalytic systems are commonly engaged to lower the energy barrier for CO₂ converting. The choices of both the applied energy and functional materials, and how they are

J. Tang, J. Tang, M. Mayyas, M. B. Ghasemian, J. Sun, M. A. Rahim, J. Yang, J. Han, R. Jalili, M. G. Saborio, Z. Cao, C. A. Echeverria, F.-M. Allieux, K. Kalantar-Zadeh
School of Chemical Engineering
University of New South Wales (UNSW)
Sydney, NSW 2052, Australia
E-mail: jianbo.tang@unsw.edu.au; k.kalantar-zadeh@unsw.edu.au

D. J. Lawes
Mark Wainwright Analytical Centre
University of New South Wales (UNSW)
Sydney, NSW 2052, Australia
T. Daeneke
School of Engineering
Royal Melbourne Institute of Technology (RMIT)
Melbourne, VIC 3001, Australia

A. Zavabeti
Department of Chemical Engineering
The University of Melbourne
Parkville, VIC 3010, Australia

J. Hamilton, V. Mitchell
Australian Synchrotron
ANSTO
Clayton, VIC 3168, Australia

A. P. O'Mullane
School of Chemistry and Physics
Queensland University of Technology (QUT)
Brisbane, QLD 4001, Australia

R. B. Kaner
Department of Chemistry and Biochemistry and California NanoSystems Institute
University of California
Los Angeles, CA 90095, USA

R. B. Kaner
Department of Material Science and Engineering
University of California
Los Angeles, CA 90095, USA

D. Esrafilzadeh
Graduate School of Biomedical Engineering
University of New South Wales (UNSW)
Sydney, NSW 2052, Australia
E-mail: d.esrafilzadeh@unsw.edu.au

M. D. Dickey
Department of Chemical and Biomolecular Engineering
North Carolina State University
Raleigh, NC 27695, USA

 The ORCID identification number(s) for the author(s) of this article can be found under <https://doi.org/10.1002/adma.202105789>.

DOI: 10.1002/adma.202105789

pooled together for CO₂ conversion govern the efficiency balances. To date, light and electricity have been extensively used as the triggering energies together with many well-known catalytic systems.^[4–8] However, in general, the existing electro- or photo-empowered CO₂ reduction systems suffer from sluggish reaction rates and high energy consumption. Additionally, there has also been no magical definitive catalyst that could synergistically operate with these energy types to carry out the conversion at low costs and high efficiencies.

Mechanical energy is easy to generate and often a waste source of energy. Except for organic synthesis and polymerization,^[9,10] mechanical energy has received little attention in catalytic systems^[11] and has not yet been utilized for CO₂ reduction. In conductive particles suspensions, the introduction of mechanical stimuli can generate triboelectrification, as a result of the frictional contact in the presence of dielectric materials.^[12]

Solid metallic catalysts have exhibited excellent performance for electrocatalytic or photocatalytic CO₂ reduction.^[13–15] However, the active sites of solid metallic catalysts can deteriorate under intense mechanical stimuli and/or be deactivated when carbonaceous materials adhere onto the catalytic sites during CO₂ reduction. In principle, the use of liquid metals, and specific solid structures, can solve these problems. Gallium (Ga)-based liquid metals have shown intriguing properties for catalysis, including tunability by the incorporation of other elements, and remarkable resistance to coking^[16–19] and also excellent mechanical tolerance. Additionally, it is known that Ga(0) can be oxidized to Ga⁺ in the presence of organic materials.^[20] In this work, we explore whether the same effect can also apply to CO₂ and whether we can find a process to reduce Ga⁺ back to Ga(0) in a closed cycle stimulated by mechanical agitation. We envision that by employing liquid-metal mixes of Ga and a compound of Ag, a closed cyclic catalytic system can be developed. This system can then convert CO₂ into value-added species in the reversible Ga–Ga⁺ cycle, which will be fully explored.

2. Results and Discussion

2.1. Assessment of CO₂ Conversion for Various Scenarios

We exploited a suspension of Ga and Ag(I) salt mixes as the precursors of the co-catalysts and ultrasound was initially employed to stimulate the CO₂ reduction. Dimethylformamide (DMF), with good stability during mechanical agitation and high CO₂ solubility of 0.14 M at 40 °C (to assure the liquid state of Ga), was chosen as the solvent.^[21] We observed that during the reaction, the CO₂ molecules near the interface of the suspended particles were reduced to form carbonaceous sheets in a process that will be detailed later.

The best outcomes were obtained when Ga and AgF were mixed in a DMF solution which also contained 0.10 M HCl to remove the native oxide on the surface of Ga. Ga and AgF were sonicated together (Figure 1a—using a probe sonicator for 30 min) to generate sub-micrometer Ga droplets of 230 nm median diameters and Ag_{0.72}Ga_{0.28} rods of micrometer/sub-micrometer lengths and median diameters of 160 nm (Figure 1b and Figure S1, Supporting Information). The characterization

outcomes revealing the elemental composition will be presented in a later section.

In the reactor, CO₂ was bubbled into DMF through a diffuser to facilitate its dissolving process (Figure 1c). The dissolved CO₂ is reduced to solid carbonaceous materials at the interface of the Ga droplets. The mechanically enforced CO₂ conversion can be scaled up using a variety of mechanical sources that produce frictional contact. To examine this prospect, CO₂ conversion by an overhead mixer was also performed and validated (Figure 1d).

Due to the ultrasmooth nature of the liquid-metal droplets, the produced carbonaceous materials on the surface are in the form of sheets.^[16,22] These low-dimensional sheets, on the non-polarized liquid-metal surface, are exfoliated during mechanical stimulation (Figure 1e).^[16,22] Most importantly, the carbon sheets migrate to the top of the reactor and can be isolated due to the density difference with reference to that of metallic components (Figure 1c,d).

The qualitative and quantitative analyses of the production of carbon, when the Ga/AgF (7.0–1.0 mass ratio) suspension in DMF is utilized in a 20 mL reactor, are presented in Figure 1f and Figure S2 in the Supporting Information. The 7.0–1.0 mass ratio and the reaction temperature were chosen according to previously optimized data for C–C bond formation reactions.^[20] Additionally, the performance of the system formed by direct alloying of Ga with silver (5.0–1.0 or 2.0–1.0 mass ratio of Ga/Ag, Figure S3e,f, Supporting Information) and different silver salts (Figure 1g–k), including AgCl, AgBr, AgI, AgOTf, AgNO₃ (also 7.0–1.0 mass ratio) were compared. The homogenous mixture (20 μL) was drop-cast onto a glass substrate and dried for Raman analysis, with the whole drop-cast region included during the Raman spectroscopy measurement (Figure S3a–d, Supporting Information). The changes in the intensity of the carbon D and G bands at 1350 and 1600 cm^{−1}, respectively, were employed to obtain the overall picture. Thermal gravimetric analyses (TGA) and gas chromatography (GC) were also conducted for comparative quantitative assessment of the solid carbon and gaseous products (Table S1, Supporting Information).

For the Ga/AgF system that exhibited the best performance, the production of carbon was observed in < 1 h of reaction (Figure 1f) and increased continuously over time according to TGA. The TGA showed that 4.95 mg of carbonaceous materials were produced per hour in a 20 mL reactor at a CO₂ flow rate of ≈10 sccm (0.027 mol h^{−1}) (Figure S2, Supporting Information). In comparison, the AgCl, AgBr, AgI, and AgOTf mixes also presented CO₂ conversion capability, but they were not as efficient as the AgF system (Figure 1g–j, for brevity only Raman spectra are shown and not TGA). With no emerging D and G bands after 5 h of reaction (Figure 1k and Figure S3e,f, Supporting Information), Ga/AgNO₃ and Ga–Ag alloys were found to be ineffective for CO₂ reduction. The reason for these different conversion activities will be discussed later.

To verify that the CO₂ reduction relies on the synergism of Ga and AgF, experiments were conducted by employing Ga and AgF separately (Figure S3g,h, Supporting Information), both of which resulted in undetectable carbon production. Also, the Ag_{0.72}Ga_{0.28} rods alone could not achieve CO₂ conversion (Figure S4, Supporting Information). We note that our attempts with other types of salts (e.g., KCl and NaCl) showed no carbon

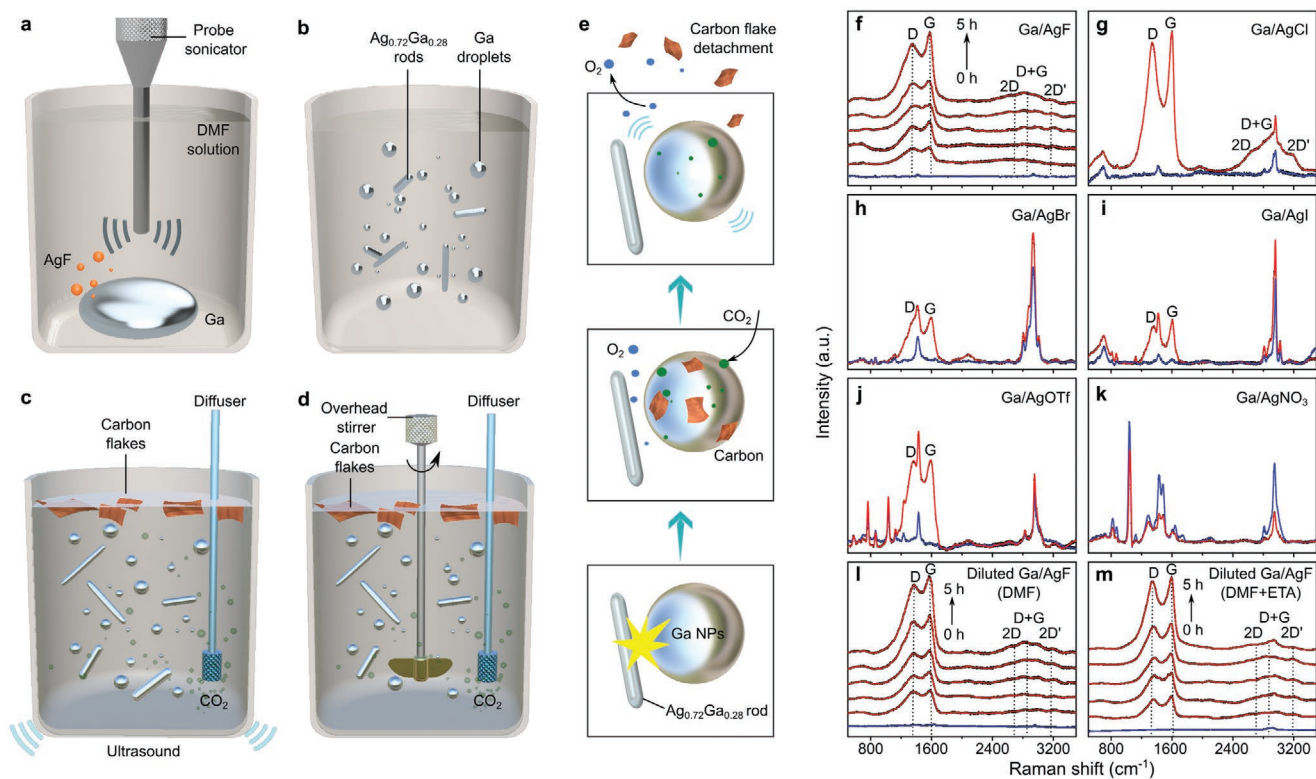


Figure 1. Schematics and Raman spectra of solid carbon produced from CO_2 using liquid metal. a–d) Schematic illustrations for the preparation of a suspension of catalyst (a,b) and the CO_2 reduction process (c,d) using different mechanical energy inputs. e) Schematic illustration of the CO_2 conversion process. The formation/detachment of the carbon flakes and the generation/escape of O_2 are indicated. f–k) Raman spectra of the samples obtained from the reaction mixes of Ga with different silver salts as precursors in DMF: f) AgF (vs time), g) AgCl, h) AgBr, i) AgI, j) AgOTf, and k) AgNO_3 . The D and G bands at 1350 and 1600 cm^{-1} , respectively, emerged after the reactions occur. l,m) Raman spectra (vs time) from the surface of mixtures from the ten times diluted reaction system (Ga and AgF mix) by employing DMF (l) and DMF+ETA (m) as the reaction solutions. The blue and red curves in (f)–(m) are Raman spectra for the samples before and after reaction, respectively.

formation, indicating the crucial role of the chosen silver salt (AgF) (Figure S3i,j, Supporting Information). Controlled N_2 bubbling also did not show any formation of carbonaceous products (Figure S3k, Supporting Information).

We explored the minimum co-catalyst mass required in the system to maintain the efficiency of CO_2 conversion. Diluting the catalyst by ten times offered nearly the same conversion efficiency, still achieving an equivalent production of 4.75 mg of carbonaceous materials per hour at ≈ 10 sccm CO_2 bubbling rate (Figure 1l and Figure S2, Supporting Information), whereas the output was dramatically reduced for dilutions of 50 or 100 times (Figure S3l,m, Supporting Information). TGA profiles are not shown for brevity.

The amount of CO_2 dissolved in solution significantly influenced the efficiency of CO_2 conversion. Ethanolamine (ETA) is a suitable choice for increasing this amount since CO_2 solubility is 5.6 m in pure ETA^[23] in comparison to 0.14 m in DMF at 40 °C. With the addition of 10 vol% ETA in DMF (referred to as DMF+ETA hereafter), CO_2 was continuously reduced with a higher efficiency, producing 7.95 mg of carbonaceous materials per hour in the same reactor at ≈ 10 sccm CO_2 bubbling rate (Figure 1m and Figure S2, Supporting Information). Interestingly, 22.2 cm^3 (9.52×10^{-4} mol) CO was also produced in 1 h (Figure S5, Supporting Information). In contrast, when dimethyl sulfoxide or H_2O were used, the efficiency was very low and

carbon products could not be quantified by TGA, owing to their limited CO_2 solubility (Figure S3n,o, Supporting Information).

2.2. Carbonaceous Materials Characterization

Carbonaceous materials produced from CO_2 were isolated for further characterization. Scanning electron microscopy (SEM) and energy-dispersive X-ray spectroscopy (EDS) analysis (Figure 2a and Figure S6a, Supporting Information) of the isolated carbonaceous materials reveal that the solid product consists of carbon and oxygen before any secondary washing, with trace quantities of the metallic species that can be easily removed. Fourier transform infrared (FTIR) spectroscopy (Figure S6b,c, Supporting Information) further confirms that the carbonaceous materials are primarily comprised of C=C and C–O bonds.^[17] Based on X-ray photoelectron spectroscopy (XPS) analysis, the C 1s region of the carbonaceous materials shows characteristic peaks of sp^2 carbon and C–O bonding, at 284.2 and 286.1 eV, respectively (Figure S6d, Supporting Information).^[24] The presence of C–O bonds is validated from the O 1s XPS region of the sample (Figure S6e, Supporting Information). Transmission electron microscopy (TEM) and selected-area electron diffraction (SAED) images demonstrate that part of the carbonaceous material is akin to that of slightly

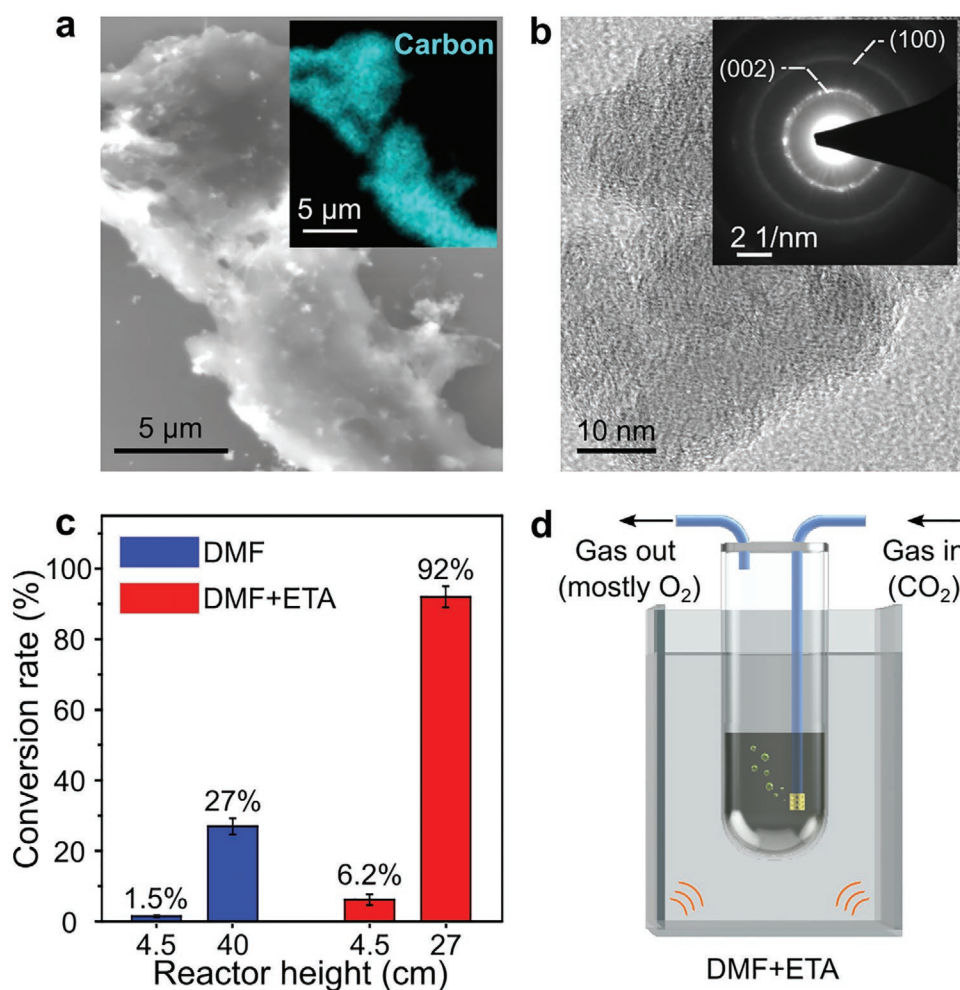


Figure 2. Characterizations of the carbonaceous products and the demonstration of the scalability of the technology. a) SEM and EDS (insert) images of the carbonaceous materials. b) TEM and SAED (insert) images of the separated carbonaceous products. c) Conversion efficiencies of CO₂ under different configurations showing the maximum efficiency of 92% for CO₂ capture and conversion in DMF+ETA case. d) Schematic representations of the scaled-up reactors for full CO₂ conversion for DMF+ETA reactors (refer to Supporting Information for the actual picture of the reactor).

crystalline graphene oxide (Figure 2b), and a certain proportion of the product exists in the amorphous state (Figure S6f, Supporting Information).

2.3. Efficiency and Energy Requirement for CO₂ Conversion

The CO₂ conversion efficiencies under different configurations were determined using TGA and GC measurements as summarized in Table S1 (see Supporting Information). The conversion efficiency is defined as (captured and reduced CO₂/total input CO₂) × 100%, which are all obtained from the optimum mix of Ga/AgF (to be explained further in the next section).

In the small-volume reactor of 20 mL and height of 4.5 cm, which was used as the characterization unit in the previous sections, the conversion efficiencies are 1.5% and 6.2%, for DMF and DMF+ETA cases, respectively (Figure 2c). To demonstrate the scalability, we increased the dimensions of the reactor (Figure 2d). When the height of the reactor was increased to

40 cm for only DMF solvent (volume of 500 mL), 27% of the input CO₂ at the flow rate of ≈8.6 sccm (0.0232 mol h⁻¹) could be continuously captured and converted (Figure 2c). Thus, when the total height of the reactor would be 148 cm, the CO₂ conversion could reach the full capacity.

The height of the reactor for near-full conversion could be significantly decreased when DMF+ETA was used as the solvent as this combination could significantly increase the CO₂ solubility. The conversion efficiency reached the unprecedented value of 92% (at the flow of ≈8.0 sccm CO₂, 0.0216 mol h⁻¹) in this case for a reactor as small as 27 cm in height and 330 mL in volume (Figure 2c, see Figure S7 for the photo of the set-up and supplementary discussion for the corresponding turnover number, Supporting Information). The amount of produced O₂ and carbonaceous materials (highly oxidized carbon), under different conditions, is presented in Figure S8 and Table S1 in the Supporting Information. To assess the stability and durability of the system, the reaction was conducted continuously for a period of over 100 h. As presented in Figures S9–S11 and Supplementary discussion in the Supporting Information, there is

no deterioration of the performance or change of the catalytic materials and solvent in the reactor.

According to these measurements, the total energies required for converting 1.0 tonne of CO₂, for DMF and DMF+ETA cases, are obtained as ≈700 kW h and ≈230 kW h (excluding the energy used for dissolving CO₂ during bubbling through diffusers), respectively (Supporting Information). In the DMF+ETA case of 92% conversion rate, the mechanical-to-chemical energy conversion efficiency is estimated to be between 53% and 79.5% (see Supplementary discussion, Supporting Information). Note that the energy cost for CO₂ purification is not considered in our calculations. An overall estimation based on the current price of electricity suggests that the operational cost of CO₂ capture and conversion using DMF+ETA is lower than any other state-of-the-art technologies.^[25–29]

We also used lower concentrations of CO₂ (20% and 6%, diluted with N₂) and introduced 5% water into the reaction system to crudely simulate commonly encountered CO₂ sources

such as flue gas or exhaust gas (see Figure S12, Table S2, and Supplementary discussion for details, Supporting Information). CO₂ conversion was observed in all cases and the small amount of water did not decrease the conversion rate. These results demonstrate the promising capability of our reaction system for low concentration CO₂ conversion without pre-purification.

2.4. Analysis of the Suspensions

To elucidate how the functional materials are formed during the probe sonication stage, the reactions between Ga and silver salts were investigated by characterizing the sonication products. Sonicating Ga with AgF (as an exemplar) forms an intermetallic phase Ag_{0.72}Ga_{0.28} (Figure 3a) and GaF₃. The existence of metallic Ag (as Ag_{0.72}Ga_{0.28}) is confirmed by the Ag 3d XPS peaks at 367.8 and 373.8 eV (Figure 3b).^[30] The metallic fluorides can be verified by the F 1s XPS peak at 684.3 eV (Figure 3c).^[31]

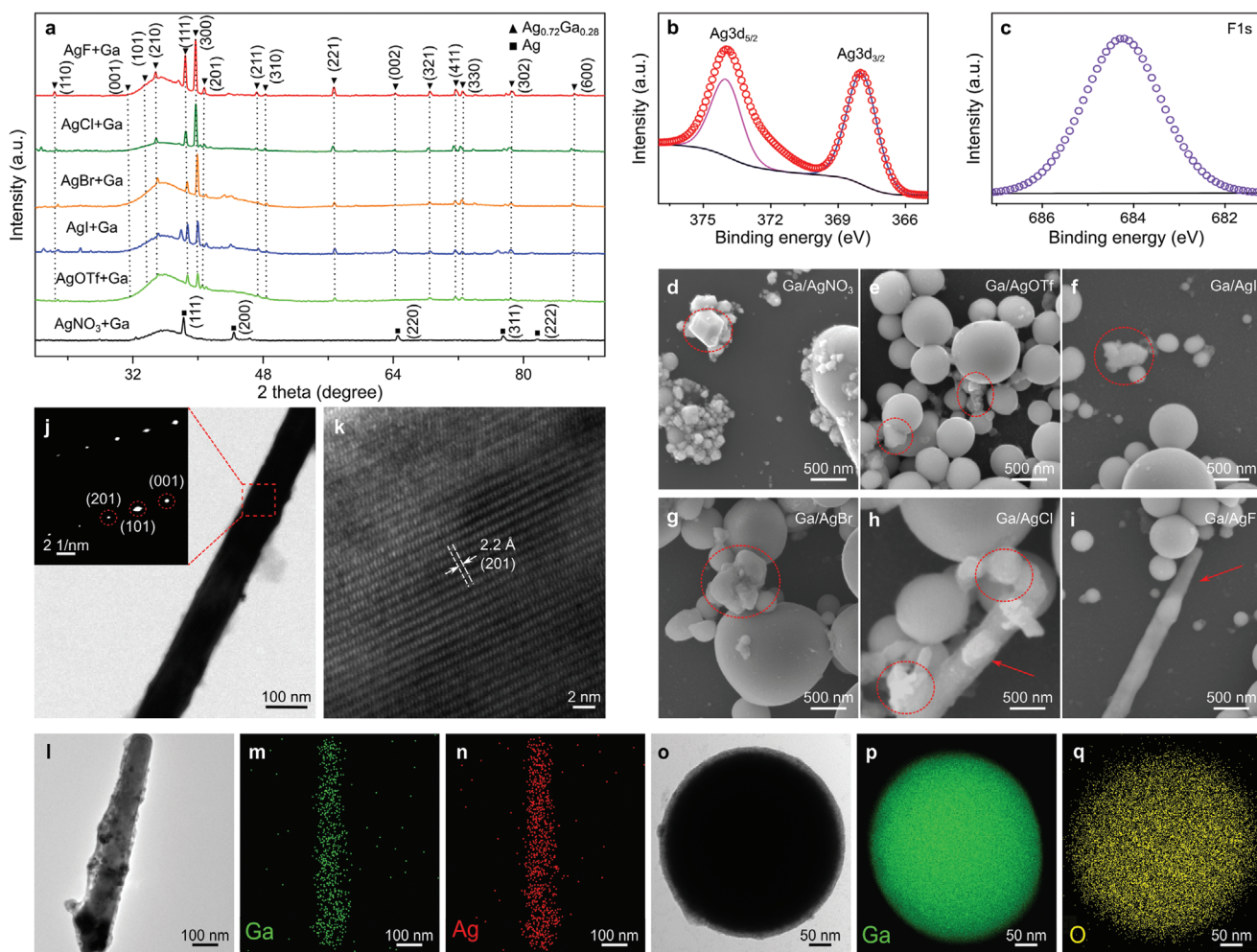


Figure 3. Characterization of the functional materials. a) XRD patterns after probe sonication by employing different silver salts with Ga as the precursors. Except for Ga/AgNO₃, the other silver salts and Ga were converted into Ag_{0.72}Ga_{0.28}. b,c) XPS analysis of the state of silver and fluoride on the surface of the mixtures after probe sonication. d–i) SEM images of the materials after probe sonication when different silver salts were used as precursors as: d) Ga/AgNO₃, e) Ga/AgOTf, f) Ga/AgBr, g) Ga/AgI, h) Ga/AgCl, and i) Ga/AgF. Ag_{0.72}Ga_{0.28} was found in the shape of rods only when AgF was used as the precursor, and some rods were also seen for the AgCl case, while Ag_{0.72}Ga_{0.28} from other silver salts have non-rod morphologies. j,k) TEM and HRTEM of Ag_{0.72}Ga_{0.28} nanorods with SAED images inserted in (j). l–q) TEM and corresponding EDS images of Ag_{0.72}Ga_{0.28} rods and Ga droplets.

The compositions and morphologies of the materials were investigated and correlated with the CO₂ reduction performance. As illustrated in Figure 3a, X-ray diffraction (XRD) patterns of Ga mixed with silver salts, which lead to CO₂ conversion (i.e., AgF, AgCl, AgBr, AgI, and AgOTf), show the presence of Ag_{0.72}Ga_{0.28} crystalline peaks. The control experiments show that Ag₂Ga particles (generated from the sonication of Ga–Ag alloy, Figure S13, Supporting Information) and Ag particle inclusions (using Ga/AgNO₃ as the precursors, Figure 3a,d) are inactive materials for CO₂ conversion. These results suggest that the formation of Ag_{0.72}Ga_{0.28} is a prerequisite for CO₂ reduction. Interestingly, the Ag_{0.72}Ga_{0.28} crystals, generated from different silver salts, show distinct morphologies (Figure 3e–i and Figure S14, Supporting Information) of particles (Figure 3e–g) or rods (Figure 3i for AgF) or a combination of both (Figure 3h for AgCl) together with the Ga spheres. The presence of only rod-shaped morphology (Figure 3i for AgF) is found to associate with an enhanced CO₂ catalytic capability. The Ga/AgF system, which generated the highest efficiency for CO₂ conversion, showed the rod-shaped Ag_{0.72}Ga_{0.28}, while Ag_{0.72}Ga_{0.28} with non-rod morphology from other silver salts (or limited rod morphology for AgCl) exhibited limited catalytic abilities. The high-resolution TEM images, SAED pattern (Figure 3j,k), and the TEM-based EDS mapping (Figure 3l–n) further confirm the existence of the Ag_{0.72}Ga_{0.28} rods and their growth direction along the [201] plane (Figure 3k). As shown in Figure 3o–q, the native oxide layer on the surface of the Ga droplets can be observed when dried for analysis. Furthermore, there were no obvious changes to the Ag_{0.72}Ga_{0.28} structures after 5 h of reaction according to both XRD (Figure S14x, Supporting Information).

The concentration of gallium and silver ions in solution during the reaction was measured by inductively coupled plasma mass spectrometry (ICP-MS; Figure S15, Supporting Information). The ion concentrations fluctuated without showing any increasing or decreasing trend, indicating that the catalysts are not consumed, and that the system is stoichiometrically stable.

2.5. Reaction Mechanism

Based on the configuration of the catalytic process, we can consider a scenario in which the interfacial charge of the Ga droplets is altered by the fast frictional contact of the Ag_{0.72}Ga_{0.28} rods under sonication. The contact instantaneously generates an ultrathin surface oxide on the Ga droplets,^[32] which leads to a localized contact electrification of the oxidized site at the Ga/DMF interface. The formation of a closed loop, by the Ag_{0.72}Ga_{0.28} rods, thereafter, initiates the CO₂ conversion. The presence of the triboelectric effect can be validated by proof-of-concept macro-sized experiments that is illustrated in Figure 4a (see discussion in the Supporting information). As can be seen, after the sharp ended electrode touches the surface of the liquid metal, immediately a large triboelectric voltage is produced (Figure 4b), which is different from the galvanic voltage of 0.88 V (Figure 4c). The formation of the oxide layer is seen in Figure 4d–g (refer to Equation (1)). When the sharp electrode detaches from the surface, the surface oxide immediately disappears (Figure 4h), demonstrating the reversibility of the system (Equation (1)). The equilibrated Ga ion concentration

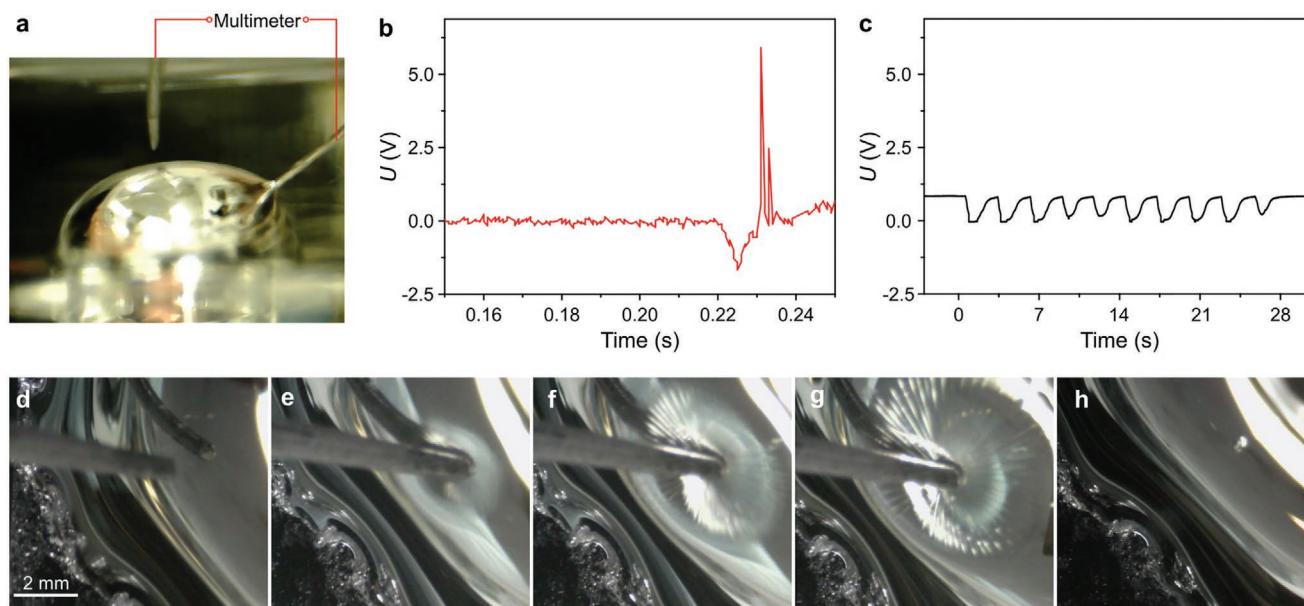


Figure 4. Voltage measurement between a Ga liquid droplet and a AgGa electrode and observation of the state of Ga surface upon the contact by a metallic needle. a) The set-up for measuring the voltage U , between the AgGa and Ga droplet in the DMF + ETA solution with the addition of HCl (0.1 M). b) The triboelectric voltage generated during the fast contact–detach process between the AgGa and Ga droplet measured at the input impedance of 25 M Ω . c) The measurements of the galvanic potential between the AgGa and Ga droplet when the AgGa was penetrated into the Ga droplets during ten repeated cycles (measured at input impedance of 1 M Ω). A large triboelectric voltage of about 5.5 V was measured between the two electrodes during their instant contact–detach, which is much higher than the galvanic potential presented in (c). d–h) The oxidation of the Ga droplet surface upon the contact–detach of a metallic needle in DMF+ETA solution with the addition of HCl (0.1 M).

(Figure S15, Supporting Information) together with the rest of the mechanism discussions, which will be presented in the following section, also suggests that the localized Ga oxidation in nanosize is reversible and Ga is not consumed during the process.



The CO₂ reduction in our system is completed through a reversible Ga–Ga⁺ cycle. Cyclic voltammetry was conducted to provide an insight into the catalytic mechanism of the Ag_{0.72}Ga_{0.28} rods via the suggested route. The results showed that, for the working electrode containing Ga droplets and Ag_{0.72}Ga_{0.28} rods as the co-contributors, Ga is oxidized to Ga⁺ at 0.18 V and then reduced to elemental gallium at –0.31 V (Figure 5a).^[33] Considering that the triboelectric process generates time-dependent voltages of several volts, the carbonaceous sheets are rapidly produced on the surface of liquid metals as we have previously demonstrated.^[34] We also note that Ga⁺ reduction was not observed when either Ga droplets (Figure 5b), Ag_{0.72}Ga_{0.28} rods (Figure 5c), or Ga droplets with nonrod morphology Ag_{0.72}Ga_{0.28} were used as the working electrode (Figure S17, Supporting Information), showing the importance of the long rods for the cyclic reaction.

To investigate the reaction mechanism, we performed a detailed assessment of the reaction intermediates and the by-products generated during CO₂ reduction. The overall reaction process in DMF is described by chemical reaction Equations (2)–(7). The equations are separated into “liquid-metal components” reactions (Equations (2)–(5)) and “solid components” reactions (Equations (6) and (7)). For the description of the liquid-metal component reactions, a series of characterizations were conducted. NMR analysis showed that the solvent DMF was not involved in the reaction (Figure S18a, Supporting Information). The CO₂ reduction is realized via the voltage provided by the nanotriboelectrochemical process on the surface of Ga liquid droplets that turn Ga into Ga⁺, while CO₂ is activated into the CO₂^{•–} radical (Equation (2), Figure 5e–g, see Figure S19, S20, and Supplementary discussion, Supporting Information). The existence of the CO₂^{•–} radical during the reaction is demonstrated by electron paramagnetic resonance (EPR), which uses 5,5-dimethyl-1-pyrroline N-oxide (DMPO) as a radical trapping agent to form DMPO–CO₂^{•–} adduct for spectroscopic analysis (Figure 5e, see Experimental Section).^[35] The CO₂ to CO₂^{•–} process is followed by the generation of the intermediates CO and O^{2–} radicals (Equation (3), see Supplementary discussion about the O^{2–} radical, Supporting Information).^[36] The former is further converted to carbonaceous materials on

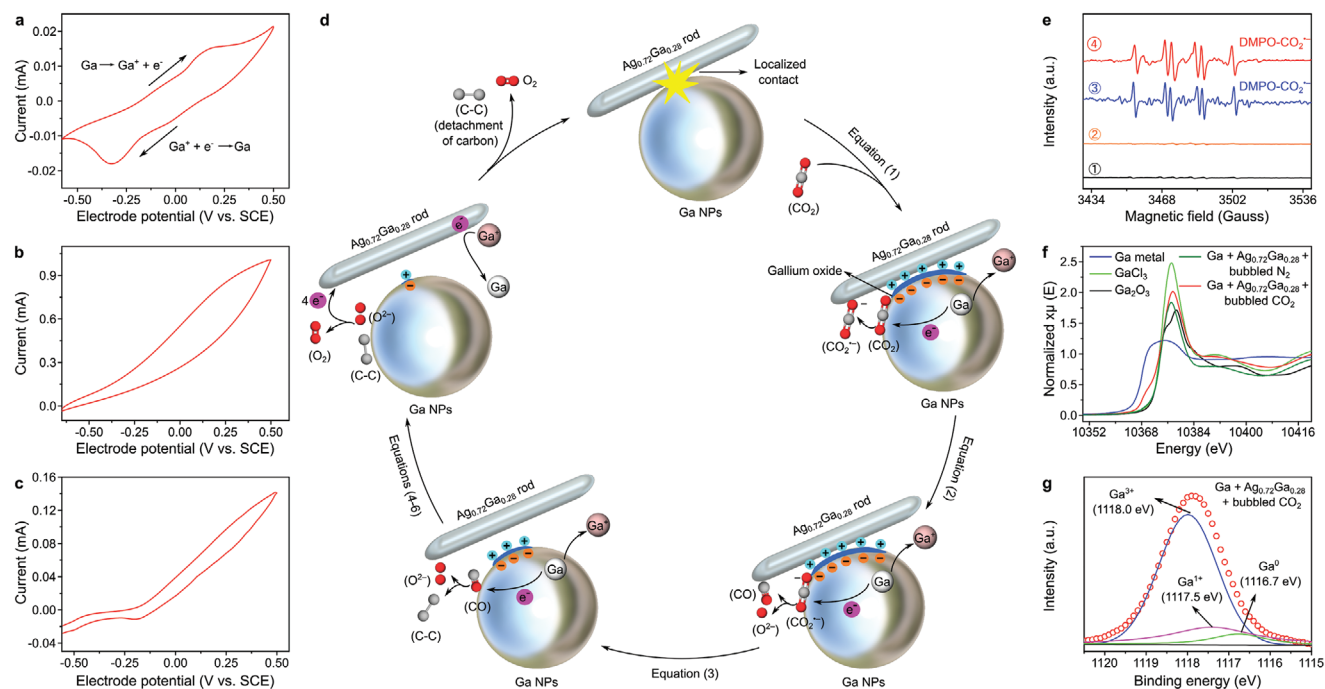
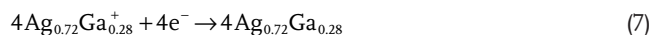


Figure 5. Reaction mechanism of CO₂ reduction. a) Cyclic voltammogram of the Ga⁺–Ga cycle with Ga droplets and Ag_{0.72}Ga_{0.28} rods as the working electrode. b,c) Cyclic voltammograms recorded with only Ga droplets and Ag_{0.72}Ga_{0.28} rods working as the functional material. d) Proposed catalytic cycle for CO₂ reduction on the surface of Ga droplets with Ag_{0.72}Ga_{0.28} rods working as the functional material. e) EPR spectra of the carbon dioxide radical (CO₂^{•–}) addition to DMPO. 1) Spectrum of DMPO added into the reaction solution for 30 min without bubbling CO₂. 2) Spectrum of DMPO added into the CO₂ bubbled reaction solution for 30 min without energy input. 3) Spectrum of DMPO–CO₂^{•–} by ultraviolet photolysis of 100 × 10^{–3} M NaHCO₂ and 100 × 10^{–6} M H₂O₂ in the presence of 50 × 10^{–3} M DMPO in Milli-Q water for 10 min, followed by the addition of photolytic 1.0 mL solution into 20 mL DMF for EPR analysis. 4) Spectrum of DMPO–CO₂^{•–} with DMPO added into the reaction solution for 30 min when CO₂ reduction is proceeding. f) XANES spectra of the reaction system containing Ga droplets and Ag_{0.72}Ga_{0.28} rods with bubbling of CO₂ and N₂, and the reference spectra for Ga metal, GaCl₃, and Ga₂O₃. g) XPS showing the Ga 2p spectrum of Ga droplets and Ag_{0.72}Ga_{0.28} rods after CO₂ conversion using Ga and AgF as the precursors. The XANES, XPS, and electrochemical analyses further prove the accuracy of Equations (1) to (6). See Supporting Information for further discussion.

the liquid-metal surface (Equation (4) which is the optimum case and it can be altered according to the C to O ratio in the obtained carbonaceous solid). The equations are as follows



The description of the “solid components” reactions is as follows. According to the cyclic voltammetry results, the oxidized Ga⁺ can be reduced to elemental Ga by receiving an electron from the Ag_{0.72}Ga_{0.28} and the Ag_{0.72}Ga_{0.28} turns into Ag_{0.72}Ga_{0.28}⁺ (Equation (6)). The catalytic cycle is closed by the electrons provided from the O²⁻ to O₂ (Equation (5)) to reduce Ag_{0.72}Ga_{0.28}⁺ back to Ag_{0.72}Ga_{0.28} (Equation (7)), where the existence of O₂ can be confirmed through GC (Figure S5 and Table S1, Supporting Information). Altogether, the Ag_{0.72}Ga_{0.28} rods remain intact (Figure S10, Supporting Information) during the process and the Ga–Ga⁺ cycle plays a crucial role as evidenced by X-ray absorption near edge structure (XANES) spectroscopy (Figure 5f),^[37,38] XPS (Figure 5g), and electrochemical analyses (Figure 5a–c)



The triboelectric potential generated during the oxide formation and reversible Ga to Ga⁺ conversion process drive the CO₂ activation and conversion. They also guarantee the reversibility of the system. For clarity, a closed loop equivalent circuit formed by Ga droplet, the reversible oxide layer, and Ag_{0.72}Ga_{0.28} rod is presented in Figure S21, Supporting Information that describes how the electrochemical system operates. The catalytic cycle of CO₂ reduction at the interface of Ga droplets is illustrated in Figure 5d. This catalytic mechanism also aligns with the DMF+ETA case, and the extra by-products are produced due to the presence of ETA that promotes the process toward CO production according to Equation (3) (Figure S5 and Figure S18b, Supporting Information).^[39] Further experiments with ¹³C labeling (Figure S22, Supporting Information),^[40] NMR (Figure S11, Supporting Information), and a control experiment of long-term N₂ bubbling only (Figure S9g, Supporting Information) were conducted to show that during the reaction the solvent remains intact and only CO₂ is the source of the observed products.

Since the reaction is activated by the triboelectric potential, other forms of mechanical stimuli can also be applied, and the system can be readily scaled up. As a demonstration, we further validate our strategy by coupling an overhead stirrer to a 50 mL reactor. We found that CO₂ conversion continuously takes place in a stable manner when the stirring speed exceeds a threshold of 200 rpm (at room temperature, Figure S23a, Supporting Information) and the conversion efficiency increases along with the increase of the stirring speed (equivalently, the mechanical

energy input) (Table S1 and Figure S23b,c, Supporting Information). The input energy and its frequency (equivalently, rotation speed during overhead stirring) were found to affect the CO₂ conversion rate as well as the structure/stoichiometry of the produced carbonaceous materials (Figure S23 and Supplementary discussion, Supporting Information).

3. Conclusion

We have demonstrated a promising mechanical-energy-induced CO₂ conversion method which operates solely with mechanical stimuli. The catalytic process was found to be mechanically enabled by co-contributors containing liquid-metal Ga droplets and resilient intermetallic Ag_{0.72}Ga_{0.28} structures. We demonstrated the crucial roles of the composition and morphology of the functional materials, as well as the importance of precursor selection for triboelectrochemical CO₂ conversion. The obtained CO₂ capture and conversion efficiency was 92% for a reactor with a height as small as 27 cm at the input CO₂ flow rate of ≈8 sccm. As one of the by-products, O₂ acts as an essential part during the CO₂ conversion process. The oxygen tolerance of our system can be an advantage when compared to other CO₂ conversion techniques which require oxygen-free environments.

The prospects of further exploring the proposed system are extensive. This methodology can be extended for large-scale systems and long-term operation by employing different forms of mechanical energies. This methodology with its remarkable capabilities provides promising prospects for future practical deployment of CO₂ conversion technologies. The carbonaceous materials presented here are produced at low costs. These by-products can be used as construction materials, fillers for various composites, supercapacitor ingredients, adsorbents for filtering, and catalyst support. Altogether, the novel concept provided by this new system offers a platform to fundamentally impact the future of carbon capture technologies and relevant industries.

4. Experimental Section

Materials: Gallium (Ga, ingot, purity: 99.99%) was purchased from Rotometals, USA, and silver powder (purity: 99.9%) was obtained from Sigma-Aldrich. All the salts, including AgF, AgCl, AgBr, AgI, AgOTf, AgNO₃, KCl, NaCl, and NaHCO₂, were obtained from Sigma-Aldrich with a purity of 99.5%. The solvents DMF (purity: 99.8%, boiling point: 153 °C), ETA (purity: ≈98%, boiling point: 170 °C), and HCl (33 wt% in water) were acquired from Chem-Supply Pty Ltd. HNO₃ (acidimetric: ≥65.0%), DMPO (purity: 99.9%), and H₂O₂ (30 wt% in water) were purchased from Sigma-Aldrich. Milli-Q water was used throughout the experiments for sample preparation and reaction.

Preparation of Functional Materials:

- 1) Silver salts as precursors: During a typical co-contributor preparation process (using AgF as an example), Ga (7.0 g) was first added into a glass vial which was pre-filled with 5.0 mL DMF solution, followed by adding HCl solution to give a final 0.10 M to remove the surface oxide layer of Ga. AgF (1.0 g) was then added to the mixture as the precursor.
- 2) Ag (150 nm particle size) as precursors: For the preparation of Ag–Ga alloy, the silver powder was added to Ga (7.0 g) in

concentrations of 2.0 and 5.0 wt%, respectively. The mixtures were ground using a mortar and pestle inside a N₂-filled glove box to minimize oxidation of the liquid metal.^[6] The grinding process, typically lasted 40 min, was stopped until the sample showed a smooth and reflective appearance.

- 3) Probe sonication procedures: The mixture from step (1) or step (2) was sonicated with a probe sonicator (VC 750, Sonics & Materials) under the protection of N₂. The sonication amplitude was set to 55%, corresponding to an ultrasonic power input of ≈410 W. The sonicator was paused for 1 s after each 9 s sonication and the total sonication time was 30 min.

CO₂ Conversion Experiment:

- 1) Bath sonication as the energy source: After the preparation of functional material, CO₂ was continuously bubbled into the reactor through a diffuser and the flow rate of CO₂ gas (10 sccm) was controlled using a gas mass flow controller (MKS, GE50A). Bath sonication (FREQ 50Hz, Unisonics) was employed as the mechanical energy source to trigger CO₂ conversion. The temperature of the reaction solution was kept around 40 °C during the 5 h reaction for the referencing reactions and longer hours for the experiments focused on longevity of the reaction. During the sonication, the system was switched off every 90 min for 1 min.
- 2) Overhead stirrer as the energy source: When CO₂ was bubbled into the reactor through a diffuser at the same rate of 10 sccm, an overhead stirrer (DLS Digital Overhead Stirrer, 120 W) was utilized as the mechanical energy source. Different rotation speeds, including 200, 300, 400, 500, and 1000 rpm, were applied for initiating the CO₂ conversion. The experiment was performed at room temperature for 24 h.

Sample Characterizations: Raman spectra were collected via a Raman spectrometer (Via Raman microscope, Renishaw) utilizing the 532 nm laser source. XPS was performed on a Thermo Scientific K-alpha X-ray spectrometer. The carbon product was studied using micro-FTIR spectroscopy, on a PerkinElmer Spectrum 100 FTIR Spectrometer which was coupled to a Spotlight 400 FTIR Imaging System with stage controller. The morphology and structure of materials were imaged by SEM (JEOL JSM-IT-500 HR). The TEM and SAED characterizations were performed on a Phillips CM200 TEM system. Both the SEM and the TEM systems were coupled with an EDS detector for elemental and compositional analysis. The crystalline phases of the samples were characterized by XRD (Philips X'Pert Pro MPD, $\lambda = 1.54 \text{ \AA}$, Cu-K α radiation). The TGA for carbonaceous material quantification was performed on a Thermogravimetric Analyzer TGA Q5000 IR. ICP-MS was performed on NexION 2000 B ICP Mass Spectrometer to determine the concentration of gallium and silver ions. EPR experiments for the detection of the CO₂^{•-} radicals were conducted on a Bruker EMX X-Band ESR Spectrometer (Bohr). NMR experiments were performed to investigate the liquid species in the solution, which was performed by using Bruker Avance III 600 MHz Cryo NMR (Ernst).

Preparation and Analysis of TGA Samples: The carbonaceous materials for the TGA experiments were separated by centrifugation. After a specific reaction time (*T*, h), the homogenous mixture from the reactor (2.0 mL) was added into a centrifuge tube followed by centrifuging at a speed of 10 000 rpm for 10 min. During this process, the suspended solid materials were separated into different layers. Most of the metallic catalysts were deposited at the bottom of the tube due to their high density, in comparison to the carbonaceous materials which remained suspended in the top layer. The centrifugation process was repeated three times and each time the carbon-containing top layer was collected. The collected materials (sample volume $V_{\text{TGA}} = 2.0 \text{ mL}$ solution during certain reaction time *T* (h)) were then dried (110 °C) to remove DMF from the samples before the TGA experiments. During the TGA experiments, the heating rate was set to 10 °C min⁻¹ and the upper temperature limit was fixed at 800 °C.

ICP-MS Samples: During the process of CO₂ reduction, 1.0 mL reaction mixture was taken as a sample every hour and then the sample

was centrifuged for 15 min at 10 000 rpm until all the suspended materials deposited at the bottom of the tube. Then, 0.20 mL clear solution was taken from the top of the sample and was heated on the hot plate until it was completely dried. Thereafter, 0.20 mL of nitric acid was added to dissolve the residue for ICP-MS.

Cyclic Voltammetry Experiments: Cyclic voltammetry experiments were conducted to investigate the roles of the Ag_{0.72}Ga_{0.28} rods during the CO₂ reduction. Ga droplets and Ag_{0.72}Ga_{0.28} rods were obtained from the Ga and AgF precursors. Then, the Ga/Ag_{0.72}Ga_{0.28} (Ag_{0.72}Ga_{0.28} in the shape of a rod) was painted on fluorine-doped tin oxide (FTO) and was baked until the material was dried and immobilized on the FTO as the working electrode. A calomel reference electrode and a gold counter electrode were used to set up a three-electrode configuration. DMF+ETA solution containing 0.10 M HCl was utilized as the electrolyte to keep the condition consistent to the reaction situation. As a comparison, Ga droplets, concentrated Ag_{0.72}Ga_{0.28} rods, and Ga/Ag_{0.72}Ga_{0.28} (Ag_{0.72}Ga_{0.28} with nonrod morphology, using Ga/AgI) were painted on FTO as the working electrode, respectively, and all other parameters were kept identical.

EPR Experiments: To provide mechanistic insights, EPR experiments were conducted to confirm the existence of the activated CO₂. DMPO is known as a standard CO₂^{•-} radical captor and the combination of DMPO with the CO₂^{•-} radical showed the characteristic signals.^[35,41] During the experiments, 20 mg DMPO was added and dissolved into 5.0 mL Milli-Q water and then 1.0 mL DMPO solution was further added into the reaction system. After bubbling CO₂ into the solution in the presence of bath sonication for 30 min, 1.0 mL reaction solution was centrifuged to remove all the suspended materials for EPR measurement. As a control, 1.0 mL DMPO solution was added into the reaction system in the process of bath sonication without bubbling CO₂.

To verify that the EPR signal obtained from this reaction system was due to the formation of CO₂^{•-}, an independent reaction involving CO₂^{•-} formation was further conducted. It was well established that the CO₂^{•-} radical was generated from NaHCO₂ and H₂O₂ under the irradiation of UV light.^[35] NaHCO₂ and 30% H₂O₂ were dissolved in 5.0 mL Milli-Q water in the concentration of 100 × 10⁻³ and 100 × 10⁻⁶ M, respectively, with the DMPO concentration being 50 × 10⁻³ M. After irradiation with UV light for 10 min, 1.0 mL photolytic solution was mixed with 20 mL DMF solution for EPR analysis to keep the condition consistent with the conditions of CO₂ conversion reaction. By comparison, the EPR spectra from the reaction system and photolytic solution were in good agreement, thereby validating the existence of CO₂^{•-} radical during CO₂ conversion reaction (Figure 5c).

XANES Samples and Experiments: The XANES experiments were performed at the XAS Beamline at the Australian Synchrotron, ANSTO Melbourne. Ga metal and Ga metal + Ag_{0.72}Ga_{0.28} samples in DMF + ETA + 25% glycerol (by volume, glycerol was required for liquid samples), bubbled with CO₂ and N₂, with and without Ga⁺ stabilizer (18-Crown-6), were tested. In addition, standards of pure gallium (pressed between kapton tape), Ga₂O₃ (prepared as a powder pellet), and GaCl₃ were measured as references for Ga⁰ and Ga³⁺. Nine samples (see Table S3, Supporting Information) were sonicated for 1 h before being sealed into aluminium sample holders between layers of kapton tape. Sealed sample holders were immersed in liquid nitrogen to freeze, then were stored on dry ice prior to analysis, and were maintained at ≈4 K in a helium atmosphere during analysis.

XAS spectra were recorded by measuring Ga-K fluorescence using a 100-element solid state HP-Ge detector (Canberra/Mirion, France). The excitation energy was selected using a Si(111) double crystal monochromator, which was calibrated at the Pt-L3 absorption edge using an inline Pt metal foil (first maximum of the first derivative at 11 564 eV). The X-ray beam was focused at the sample position and slits were used to reduce the beam size to an ≈1 mm spot. Short, repeat XAS scans of Sample 3 were performed to determine that the materials were sufficiently impervious to X-ray exposure for at least several minutes, thus permitting adequate XAS analyses to be conducted for the purpose of this project. XANES scans were then collected with a count time of 2 s for each energy step in the pre-edge and XANES region, with 10 eV

steps in the pre-edge region of the XAS spectra (10 167–10 347 eV), 0.25 eV steps in the XANES region (10 347–10 417 eV). In the extended X-ray absorption fine structure region spectra were collected, in steps of 0.035k to a maximum of 10k, with count time increasing linearly from 2 up to 4 s at the end of the energy range. Multiple scans were collected for each sample. Data were preprocessed using Sakura (in-house program) and the Athena program for scan averaging, background subtraction, and edge-height normalization (Ravel and Newville, 2005). Periodically throughout the experiment, transmission scans were collected of the in-line Re foil.

Supporting Information

Supporting Information is available from the Wiley Online Library or from the author.

Acknowledgements

This work was supported by the Australian Research Council (ARC) Laureate Fellowship grant (FL180100053), the ARC Center of Excellence FLEET (CE170100039), and Chevron. The authors thank Dr. Yin Yao, Dr. Sean Lim of the Electron Microscope Unit within the Mark Wainwright Analytical Centre at UNSW Sydney, and Dr. Donald Thomas of the Spectroscopy Laboratory and the Nuclear Magnetic Resonance Facility for their technical assistance.

Conflict of Interest

The authors declare no conflict of interest.

Data Availability Statement

Research data are not shared.

Keywords

CO₂ conversion, liquid metals, mechanical energy, triboelectrochemical reactions

Received: July 27, 2021
Revised: September 23, 2021
Published online:

- [1] S. Mukherjee, N. Sikdar, D. O'Nolan, D. M. Franz, V. Gascón, A. Kumar, N. Kumar, H. S. Scott, D. G. Madden, P. E. Kruger, B. Space, M. J. Zaworotko, *Sci. Adv.* **2019**, 5, eaax9171.
- [2] F. P. García de Arquer, C.-T. Dinh, A. Ozden, J. Wicks, C. McCallum, A. R. Kirmani, D.-H. Nam, C. Gabardo, A. Seifitokaldani, X. Wang, Y. C. Li, F. Li, J. Edwards, L. J. Richter, S. J. Thorpe, D. Sinton, E. H. Sargent, *Science* **2020**, 367, 661.
- [3] S. Gao, Y. Lin, X. Jiao, Y. Sun, Q. Luo, W. Zhang, D. Li, J. Yang, Y. Xie, *Nature* **2016**, 529, 68.
- [4] C. W. Li, J. Ciston, M. W. Kanan, *Nature* **2014**, 508, 504.
- [5] X. Li, Y. Sun, J. Xu, Y. Shao, J. Wu, X. Xu, Y. Pan, H. Ju, J. Zhu, Y. Xie, *Nat. Energy* **2019**, 4, 690.
- [6] Y. Wu, Z. Jiang, X. Lu, Y. Liang, H. Wang, *Nature* **2019**, 575, 639.
- [7] S. Nahar, M. F. M. Zain, A. A. H. Kadhum, H. A. Hasan, M. R. Hasan, *Materials* **2017**, 10, 629.
- [8] X. Liu, J. Xiao, H. Peng, X. Hong, K. Chan, J. K. Nørskov, *Nat. Commun.* **2017**, 8, 15438.
- [9] M. A. Stuart, W. T. Huck, J. Genzer, M. Muller, C. Ober, M. Stamm, G. B. Sukhorukov, I. Szleifer, V. V. Tsukruk, M. Urban, F. Winnik, S. Zauscher, I. Luzinov, S. Minko, *Nat. Mater.* **2010**, 9, 101.
- [10] T. Gan, S. Handschuh-Wang, W. Shang, J. Shen, L. Zhu, Q. Xiao, S. Hu, X. Zhou, *Macromol. Rapid Commun.* **2019**, 40, 1900537.
- [11] G.-F. Han, F. Li, Z.-W. Chen, C. Coppex, S.-J. Kim, H.-J. Noh, Z. Fu, Y. Lu, C. V. Singh, S. Siahrostami, Q. Jiang, J.-B. Baek, *Nat. Nanotechnol.* **2021**, 16, 325.
- [12] M. Sun, Q. Lu, Z. L. Wang, B. Huang, *Nat. Commun.* **2021**, 12, 1752.
- [13] M. Asadi, B. Kumar, A. Behranginia, B. A. Rosen, A. Baskin, N. Reprin, D. Pisasale, P. Phillips, W. Zhu, R. Haasch, R. F. Klie, P. Kral, J. Abiade, A. Salehi-Khojin, *Nat. Commun.* **2014**, 5, 4470.
- [14] H. Li, P. Wen, D. S. Itanze, Z. D. Hood, X. Ma, M. Kim, S. Adhikari, C. Lu, C. Dun, M. Chi, Y. Qiu, S. M. Geyer, *Nat. Commun.* **2019**, 10, 5724.
- [15] C. G. Morales-Guio, E. R. Cave, S. A. Nitopi, J. T. Feaster, L. Wang, K. P. Kuhl, A. Jackson, N. C. Johnson, D. N. Abram, T. Hatsukade, C. Hahn, T. F. Jaramillo, *Nat. Catal.* **2018**, 1, 764.
- [16] D. Esrafilzadeh, A. Zavabeti, R. Jalili, P. Atkin, J. Choi, B. J. Carey, R. Brkljaca, A. P. O'Mullane, M. D. Dickey, D. L. Officer, D. R. MacFarlane, T. Daeneke, K. Kalantar-Zadeh, *Nat. Commun.* **2019**, 10, 865.
- [17] D. A. Torelli, S. A. Francis, J. C. Crompton, A. Javier, J. R. Thompson, B. S. Brunshwig, M. P. Soriaga, N. S. Lewis, *ACS Catal.* **2016**, 6, 2100.
- [18] M. Losurdo, A. Suvorova, S. Rubanov, K. Hingerl, A. S. Brown, *Nat. Mater.* **2016**, 15, 995.
- [19] E. J. Markvicka, M. D. Bartlett, X. Huang, C. Majidi, *Nat. Mater.* **2018**, 17, 618.
- [20] B. Qin, U. Schneider, *J. Am. Chem. Soc.* **2016**, 138, 13119.
- [21] M. Jitaru, *J. Univ. Chem. Technol. Metall.* **2007**, 42, 333.
- [22] T. Daeneke, K. Khoshmanesh, N. Mahmood, I. A. de Castro, D. Esrafilzadeh, S. J. Barrow, M. D. Dickey, K. Kalantar-Zadeh, *Chem. Soc. Rev.* **2018**, 47, 4073.
- [23] J.-Y. Park, S. J. Yoon, H. Lee, *Environ. Sci. Technol.* **2003**, 37, 1670.
- [24] L. Chen, Z. Xu, J. Li, B. Zhou, M. Shan, Y. Li, L. Liu, B. Li, J. Niu, *RSC Adv.* **2014**, 4, 1025.
- [25] K. Z. House, A. C. Baclig, M. Ranjan, E. A. van Nierop, J. Wilcox, H. J. Herzog, *Proc. Natl. Acad. Sci. USA* **2011**, 108, 20428.
- [26] A. Kätelhön, R. Meys, S. Deutz, S. Suh, A. Bardow, *Proc. Natl. Acad. Sci. USA* **2019**, 116, 11187.
- [27] D. W. Keith, G. Holmes, D. St. K. Angelo, Heidelberg, *Joule* **2018**, 2, 1573.
- [28] R. Sen, A. Goepfert, S. Kar, G. K. S. Prakash, *J. Am. Chem. Soc.* **2020**, 142, 4544.
- [29] R.-P. Ye, J. Ding, W. Gong, M. D. Argyle, Q. Zhong, Y. Wang, C. K. Russell, Z. Xu, A. G. Russell, Q. Li, M. Fan, Y.-G. Yao, *Nat. Commun.* **2019**, 10, 5698.
- [30] J. Zhang, Y. Li, Y. Zhang, M. Chen, L. Wang, C. Zhang, H. He, *Sci. Rep.* **2015**, 5, 12950.
- [31] Y. Li, M. Bettge, J. Bareño, S. E. Trask, D. P. Abraham, *J. Electrochem. Soc.* **2015**, 162, A7049.
- [32] J. Tang, S. Lambie, N. Meftahi, A. J. Christofferson, J. Yang, M. B. Ghasemian, J. Han, F.-M. Allieux, M. A. Rahim, M. Mayyas, T. Daeneke, C. F. McConville, K. G. Steenbergen, R. B. Kaner, S. P. Russo, N. Gaston, K. Kalantar-Zadeh, *Nat. Nanotechnol.* **2021**, 16, 431.
- [33] A. J. Bard, R. Parsons, J. Jordan, *Standard Potentials in Aqueous Solutions*, IUPAC, New York, USA **1985**.
- [34] M. Mayyas, H. Li, P. Kumar, M. B. Ghasemian, J. Yang, Y. Wang, D. J. Lawes, J. Han, M. G. Saborio, J. Tang, R. Jalili, S. H. Lee,

- W. K. Seong, S. P. Russo, D. Esrafilzadeh, T. Daeneke, R. B. Kaner, R. S. Ruoff, K. Kalantar-Zadeh, *Adv. Mater.* **2020**, *32*, 2001997.
- [35] F. A. Villamena, E. J. Locigno, A. Rockenbauer, C. M. Hadad, J. L. Zweier, *J. Phys. Chem. A* **2006**, *110*, 13253.
- [36] H. V. Ijije, R. C. Lawrence, G. Z. Chen, *RSC Adv.* **2014**, *4*, 35808.
- [37] G. D. Meitzner, E. Iglesia, J. E. Baumgartner, E. S. Huang, *J. Catal.* **1993**, *140*, 209.
- [38] E. J. M. Hensen, M. García-Sánchez, N. Rane, P. C. M. M. Magusin, P.-H. Liu, K.-J. Chao, R. A. van Santen, *Catal. Lett.* **2005**, *101*, 79.
- [39] S. Zhang, P. Kang, S. Ubnoske, M. K. Brennaman, N. Song, R. L. House, J. T. Glass, T. J. Meyer, *J. Am. Chem. Soc.* **2014**, *136*, 7845.
- [40] R. Keiner, T. Frosch, T. Massad, S. Trumbore, J. Popp, *Analyst* **2014**, *139*, 3879.
- [41] Z. Barbieriková, D. Dvoranová, V. Brezová, *Catal. Today* **2018**, *313*, 106.